View metadata, citation and similar papers at core.ac.uk

brought to you by CORE

provided by University of Strathclyde Institutional Repository


Strathprints Institutional Repository

Stack, Margaret and Abdelrahman, Shehab and Jana, Buddhadev (2010) *Some perspectives on modelling the effect of temperature on the erosion-corrosion of Fe in aqueous conditions.* Tribology International, 43 (12). pp. 2279-2297. ISSN 0301679X

Strathprints is designed to allow users to access the research output of the University of Strathclyde. Copyright © and Moral Rights for the papers on this site are retained by the individual authors and/or other copyright owners. You may not engage in further distribution of the material for any profitmaking activities or any commercial gain. You may freely distribute both the url (http://strathprints.strath.ac.uk/) and the content of this paper for research or study, educational, or not-for-profit purposes without prior permission or charge.

Any correspondence concerning this service should be sent to Strathprints administrator: mailto:strathprints@strath.ac.uk

http://strathprints.strath.ac.uk/

Stack, M.M. and Abdelrahman, M.S. and Jana, B. (2010) Some perspectives on modelling the effect of temperature on the erosion-corrosion of Fe in aqueous conditions. Tribology International . ISSN 0301679X

http://strathprints.strath.ac.uk/20222/

This is an author produced version of a paper published in Tribology International . ISSN 0301679X. This version has been peer-reviewed but does not include the final publisher proof corrections, published layout or pagination.

Strathprints is designed to allow users to access the research output of the University of Strathclyde. Copyright © and Moral Rights for the papers on this site are retained by the individual authors and/or other copyright owners. You may not engage in further distribution of the material for any profitmaking activities or any commercial gain. You may freely distribute both the url (http://strathprints.strath.ac.uk) and the content of this paper for research or study, educational, or not-for-profit purposes without prior permission or charge. You may freely distribute the url (http://strathprints.strath.ac.uk) of the Strathprints website.

Any correspondence concerning this service should be sent to The Strathprints Administrator: eprints@cis.strath.ac.uk

# Some perspectives on modelling the effect of temperature on the erosion-corrosion of Fe in aqueous conditions

M. M. Stack, S.M. Abdelrahman and B.D. Jana

## Abstract

In this paper, a model is generated of the effect of temperature on the erosion-corrosion of Fe in aqueous conditions, for room temperature to 373K. The results indicate how the transition from active to passivation dominated regimes for Fe are favoured as the temperature is increased. 2D and 3D maps are constructed showing the transitions between erosion-corrosion regimes.

Keywords: Erosion-corrosion maps, CFD, slurry flow, multiphase flow, elevated temperature.

## 1. Introduction

Wastage as a result of erosion-corrosion occurs in many environments ranging from off-shore environments to health care and food industries. Many erosion models are available in the literature and these are dependent on the target material, the erodent particle, and the carrier fluid [1, 2]. Although various algorithms have been developed, few account for the effect of the temperature rise on the mechanism of the erosion process [3, 4, 5]. This is partly due to the differential effects of the temperature response for each material [6].

As the temperature rises, the carrier fluid viscosity decreases, leading to an increase in the Reynolds number. Consequently, the erosion increases. On the other hand, temperature has a significant effect on the yield strength, elasticity, heat capacity and hardness of the target material, thus leading in turn to an additional effect on the mechanical resistance of the material to particle impact [7, 8].

The corrosion process is also affected by the temperature rise. The current density is a function of the Tafel coefficients, which are affected by the solution temperature [9, 10]. Temperature also influences the stability region for the passive reaction. Cubiccioti [11] investigated the effect of the temperature rise on the E-pH diagram for stainless steel alloy, at room temperature and at 573K. The results showed an increase in the passivation reaction area along the diagram as the temperature increased, and a decrease in the dissolution and immunity region area.

Erosion-corrosion maps have been developed [12, 13] for pure metals and steel mild steel as a function of particle velocity and temperature. A recent development [14] introduced a new methodology to combine the concept of the erosion-corrosion map in 2-D dimensions with CFD modelling techniques. This technique facilitates the superimposition of 3-D erosion-corrosion maps on the surfaces of the component under investigation.

In this work, the effect of temperature on erosion-corrosion maps was studied. 2D and 3D erosion-corrosion maps were generated for mild steel (Fe). The limitations of such approach, together with future directions for the work, are discussed in this paper.

## 2. Methodology

To simplify the modeling process, various assumptions have been already summarised in previous study [15] and [14]. The validation of the CFD simulation for the erosion prediction at ambient temperature was presented in [14], where the simulation is compared with the experimental and simulation results in [16].

### *2.1 Erosion models*

#### *2.1.1. Erosion models for 2-D map construction*

The model of Sundararajan and Shewmon [17] is used in this work with some adaptation to account for the effect of temperature rise on the surface of the material used (Fe). The Sundararajan and Shewmon model is based on the so called the localisation deformation during

single impact. The model can predict the erosion rates at normal impact. The effects of the target material mechanical properties are also included. The erosion rate is expressed in term of the mass removed from the target material per unit mass of ingested particle and is given as [17]:

$$K_{eo} = \frac{0.65\, c\ \rho_p^{\,0.25} V_p^{\,3.5}}{C_p(T)\, T_m^{\,0.75}\, H_s(T)^{0.25}} \tag{1}$$

To determine the erosion rate as a standard unit; i.e. [g $cm^{-2}$ $s^{-1}$], it is necessary to multiply equation 1 with the particle flux [15] in [g $cm^{-2}$ $s^{-1}$]:

$$flux_p = 100 c_p V_p \tag{2}$$

Thus, rearranging, an expression for the pure erosion rate ($K_{eo}$) in [g $cm^{-2}$ $s^{-1}$]:

$$K_{eo} = \frac{0.65\, c\ \rho_p^{\,0.25} V_p^{\,3.5}}{C_p(T)\, T_m^{\,0.75}\, H_s(T)^{0.25}} \tag{3}$$

The metal surface mechanical properties are affected by the temperature rise. Sheldon et al. [18] related the yield strength with the Vickers hardness number by the following empirical relation:

$$H_s(T) = 2.7\, \sigma_y(T) \tag{4}$$

Nho [19] listed the effect of elevated temperature on the hardness of various carbon and stainless steel alloys. Das et al. [20] used the data in Shida et al. [21] to propose polynomial relationships for various materials to accurately relate the yield strength and the material temperature. A correlation relation for the carbon steel is given, based in these data as follows [20]:

$$Y(T) = 9.81\left(2\times10^{-5}T^2 - 0.0353\,T + 30.871\right) \tag{5}$$

Thus, the target material hardness can be related to the operating temperature as:

$$H_s(T) = 26.487\left(2\times10^{-5}T^2 - 0.0353\,T + 30.871\right) \tag{6}$$

The specific heat of the target material is also influenced by the temperature rise. From the available standard data for Fe [22], the following polynomial function can be created to represent this change:

$$C_p(T) = 17.905\,(2.038\times10^{-12}T^5 - 4.66\times10^{-9}T^4 + 4.22\times10^{-6}T^3 - 1.87\times10^{-3}T^2 + 0.432T - 16.77) \quad (7)$$

Therefore, we can use equations 6 and 7, to account for the temperature effect of the target material on its mechanical properties in the Sundararajan first model (equation 1).

*2.1.2 Erosion models for 3D map construction*

In modelling the erosion rates at any impact angle, the second erosion model of Sundararajan [23] was found to be suitable for this new method, but also needs some adaption to account for the effect of temperature rise on the surface of the material used. The model can predict the erosion rates at different impact angles and for different particle shape. It is split into two expressions; one is for the normal impact, and the other is for the oblique impact, and is summarised here as follows; for erosion by deformation [23]:

$$Er_{def} = \frac{5.5\times10^{-2}}{(T_m - 436)^{0.75}} \frac{2^{n_c}\bar{f}_t V^2 \sin^2\alpha\,(1-e^2)}{n_c C_p} \quad (8)$$

for erosion by cutting:

$$Er_{cut} = \frac{5.5\times10^{-2}}{(T_m - 436)^{0.75}} \frac{(n_c+1)\left(\frac{\mu}{\mu_f}\right)\left(2-\frac{\mu}{\mu_f}\right)V^2\cos^2\alpha}{(1+\lambda)2^{2-n_c}\,n_c\,C_p} \quad (9)$$

where:

$$\mu_f = \frac{1}{(1+\lambda)(1+e)\tan\alpha} \quad (10)$$

The normal and tangential coefficient of restitution can be related to the impact angle through the semi-empirical relation [24]:

$$e_n = 0.988 - 0.78\,\alpha + 0.19\,\alpha^2 - 0.024\,\alpha^3 + 0.027\,\alpha^4 \quad (11)$$

and:

$$e_t = 1.0 - 0.78\,\alpha + 0.84\,\alpha^2 - 0.21\,\alpha^3 + 0.028\,\alpha^4 - 0.022\,\alpha^5 \quad (12)$$

It can also be related to the target material properties as [15]:

$$e = \frac{1.36\, H_s^{0.625}}{E_e^{0.5}\, \rho_p^{0.125} V^{0.25}} \tag{13}$$

where the elastic modulus of collision (or reduced modulus of elasticity) (Ee) can be given by [25]:

$$E_e = \frac{E_t E_p}{\left[E_p\left(1-\nu_t^2\right)+E_t\left(1-\nu_p^2\right)\right]} \tag{14}$$

Eraslan and coworkers [26, 27, 8] have used experimental data of Noda [28] to model the dependency of the mechanical properties of steel on temperature. They used a nonlinear fitting formulae for the experimental data and assumed constant Poisson ratio in a temperature range from 273 – 673[K]. This assumption was found to hold for most of the engineering materials such as steels. The modulus of elasticity is given as a function of temperature from as:

$$E = E_o\left[1+\frac{\left(T-273.16\right)}{T_1 \ln\left(T/T_2\right)}\right] \tag{15}$$

where $E_o$= 200 [$GPa$], $T_1$= 2000 [$^oC$] and $T_2$= 1100 [$^oC$].

The effect of the fluid temperature rise can be estimated by its influence in the fluid viscosity and density. A curve fitting was used to fit the available data [29] for the density and viscosity change to account for their variation with the temperature rise in [K]. For the density of water:

$$\rho_l\left(T\right) = 1.65\times10^{-5} T^3 - 0.02 T^2 + 7.01 T + 207.51 \tag{16}$$

and for the water viscosity variation with temperature:

$$\mu_l\left(T\right) = 2.4\times10^{-5}\left[10^{\frac{247.8}{(T-140)}}\right] \tag{17}$$

Figure 1 and 2 show the variation of the viscosity and density of water with temperature and their curve fitting using the above two expressions. Equations (16, 17) were used in the CFD simulation to calculate the water density at the temperature range given.

## *2.2 Slurry flow models*

A dilute slurry flow of water-alumina sand particles with assumed uniform size of 10-3[m] and volume fraction of 0.1 is ingested through a pipe bend inlet with bore diameter D equal to 0.078[m] and (Rc D-1) ratio of 1.2. All CFD simulations were made by FLUENT ver.6.3 [30], which uses a finite element based finite volume method to solve the flow governing equations. Table 2 summarises the equations and operating and boundary conditions used in this study while Table 3 lists the mechanical and physical properties for the slurry and target material. A structured grid is performed in the near walls; for the bulk flow region, an unstructured grid was used. The imbalance between the mass flow rates in the exit boundary and the inlet one was computed to ensure mass continuity and found to be $1.144 \times 10^{-5}$ [kg s-1]. To validate the CFD analysis, an erosion rate comparison with the case study [31] was performed, Table 4. The validation simulation was made for SS304L stainless steel alloy using the Forder erosion model [24] as in [31]. The results in the present study were simulated for mild steel using Sundararajan's second model [23].

## *2.3 Corrosion models*

### *2.3.1 Active corrosion models*

Corrosion in steel is governed by several factors but mainly by the applied conditions of the solution alkalinity measured by pH scale and applied potential within the chemical reaction [32]. These are the factors that determine the corrosion process if it is in the dissolution or the passivation region, according to E-pH diagram for the Fe. Thus, to investigate the effect of the temperature rise on the corrosion rates, it is necessary to study the temperature rise effects on the E-pH diagram of the Fe.

Figure 3(a-d) shows the simplified E-pH diagrams for Fe at various temperatures ranging from 298 to 363 [K] respectively, showing how dissolution and passivation regions change with the temperature rise. The main electrochemical reactions equations involved are represented by the boundary lines numbered in Figure 3 (a), and are listed as follows [15]:

Line 1: $2e^- + Fe^{2+} = Fe$ (18)

Line 2: $e^- + Fe^{3+} = Fe^{2+}$

(19)

Line 3: $Fe_2O_3 + 6\,H^+ + 2\,e^- = 2\,Fe^{2+} + 3\,H_2O$

(20)

Line 4: $Fe_2O_3 + 6H^+ + 6e^- = 2\,Fe + 3\,H_2O$

(21)

Line 5: $2Fe^{3+} + 3H2O = Fe2O3 + 6H^+$

(22)

In order to construct the 2D erosion-corrosion maps correctly, these lines must be represented mathematically as a function of the applied potential and pH variables. This can be done by computing the thermodynamics that govern each electrochemical reaction. The equation of every line at the given temperature levels is listed in table 1. These lines represent the transition between dissolution, passivation and immunity regions.

The corrosion rate is mainly characterised by the summation between the pure corrosion rates ($K_{co}$), which can be neglected because it is assumed to be very low; and the contribution of erosion to the corrosion process denoted by ($\Delta K_c$) (also known as erosion enhanced corrosion) in the passive region. Corrosion rates in the dissolution region can be estimated by neglecting ($\Delta K_c$) (because these are assumed to be low) and calculating the net current density [A cm-2] from the Butler-Volmer equation which is dependent on the temperature. Equation 23 can be thus given as:

$$i_{anet} = i_o \left[ \exp\left( \frac{\beta\, z_m\, Fr\left(E_{ap} - E_o\right)}{R_o\, T} \right) - \exp\left( \frac{-(1-\beta)\, z_m\, Fr\left(E_{ap} - E_o\right)}{R_o\, T} \right) \right] \qquad (23)$$

The dissolution rate can be expressed by Faraday law:

$$K_c = K_{co} = \frac{RAM\; i_{anet}}{z_m\, Fr} \qquad (24)$$

The Butler-Volmer equation is used in modelling the dissolution corrosion rate in both 2D and 3D erosion-corrosion maps.

*2.3.2 Repassivation models for 2D maps*

In the case of passivation region, the passivation process prevents pure corrosion from further occurring, and the total corrosion rate can be simplified to the amount of passive film removal (i.e. $K_{co} \approx 0$). Tirupataiah et al. [33] developed a simple expression for the crater diameter by equating the kinetic energy of the incident particle with the energy required to form a crater. Based on Tirupatiah's work, previous work by the current group [34, 15] derived a formula for predicting the growth of the passive film at normal impacts, expressed in [g $cm^{-2}$ $s^{-1}$]. This is given as:

$$K_c = \Delta K_c = \frac{86.0\,\rho_s\, h\, c\, V_p^{\,2}}{r_p\,\rho_p^{0.5}\,H_s\,(T)^{0.5}} \tag{25}$$

Although the growth of the passive layer is dependent of the operating temperature, as discussed in [13, 12], it is assumed that the passive film is instantaneously remove by solid particle impacts. Therefore, the time interval between impacts, which allow more oxide layer formation, is assumed to be very low. Thus, the layer removed can be estimated as a linear function of over-potential only as mentioned in [35]:

$$\overline{h} = \overline{h}_o + 3\times10^{-9}\left(E_{ap} - E_o\right) \tag{26}$$

and $\overline{h}_o = 10^{-9}$ [m].

It is acknowledged that this is a simple model. Its use may be restricted at elevated temperature because of the increase in the rate of formation of the oxide layer at elevated temperatures. However, it is assumed here that the erosion and corrosion rates are independent of time. This assumption discounts the effect of the time interval between impacts. The time interval between impacts is very important factor in the erosion-corrosion process, as in the passive region, it determines the film thickness and growth kinetics [13]. However, for this study, as the thickness

of the passive film is assumed to be in the order of nanometres [35, 36], significant increase in film thickness is not considered for long intervals between impacts.

*2.3.3 Repassivation models for3D maps*

The passivation model developed in [14] is used to estimate the additive effect (Kc). It should be noted that the effect of temperature is only apparent in the reduction of the target material hardness. The erosion rate is given as:

$$\Delta K_c = \pi \, \overline{k} \, \overline{h} \, \rho_f \, d_p^2 \left[ \frac{\rho_p \left(1 - e^2\right)}{6 H_s} \right]^{0.5} \left(V \, \sin \alpha_1\right) \tag{27}$$

The unit given for the erosion model by equation 27 is [kg impact$^{-1}$]. To convert to [kg m$^{-2}$ s$^{-1}$], equation 27 is multiplied by the particle impact flux as outlined in [15]. This can be varied according to the erosion-corrosion process being modelled. For example, if the flow is homogeneous (constant particle concentration), particle impact frequency may be given as [37]:

$$I_p = \frac{c_p V_p \sin \alpha}{m_p} \tag{28}$$

Converting to [kg m$^{-2}$ s$^{-1}$] using equation 28; the passive layer erosion model will be:

$$\Delta K_c = \frac{\pi}{m_p} c_p \, \overline{k} \, \overline{h} \, \rho_f \, d_p^2 \left[ \frac{\rho_p \left(1 - e^2\right)}{6 H_s} \right]^{0.5} \left(V_p \sin \alpha_1\right)^2 \tag{29}$$

The constant (k) is defined as the mass ratio between the metal and its oxide created during the corrosion reaction multiplied by the number of moles of metal involved in the reaction, and is related to (k2) in [15]; by definition as: ($k = k_2/2$).

## *2.4 Erosion-corrosion mapping*

The total wear can be estimated as the summation of the erosion and corrosion rates and is given by:

$$K_t = K_c + K_e \tag{30}$$

where

$$K_e = K_{eo} + \Delta K_e \tag{31}$$

and

$$K_c = K_{co} + \Delta K_c \tag{31}$$

In the active regions, the erosion enhanced corrosion $\Delta K_c$ and corrosion enhanced erosion $\Delta K_e$ are neglected while in passive regions, the pure corrosion is much lower than the erosion enhanced corrosion. hence, in the active regions, the total wear is given by:

$$K_t = K_{eo} + K_{co}$$

(32)

and in passive regions the total wear may be given as:

$$K_t = K_{eo} + \Delta K_c \tag{33}$$

The regime boundaries needed for constructing the regime maps on the interior surfaces of the pipe are defined by the ratio $K_c/K_e$. and are useful in determining the transition regimes at a given applied pH and applied potential.

$$\frac{K_c}{K_e} < 0.1 \qquad \text{(Erosion dominated)} \tag{34}$$

$$0.1 \le \frac{K_c}{K_e} < 1 \qquad \text{(Erosion-Corrosion dominated)} \tag{35}$$

$$1 \le \frac{K_c}{K_e} < 10 \qquad \text{(Corrosion-Erosion dominated)} \tag{36}$$

$$\frac{K_c}{K_e} \geq 10 \qquad \text{(Corrosion- dominated)} \qquad (37)$$

The transition boundaries for the wastage maps:

$$K_t < 1 \ [mm\ year^{-1}] \quad \text{(low wastage)} \qquad (38)$$

$$1 \leq K_t < 10 \quad [mm\ year^{-1}] \quad \text{(medium wastage)} \qquad (39)$$

$$K_t \geq 10 \quad [mm\ year^{-1}] \quad \text{(high wastage)} \qquad (40)$$

## 3. Results

The erosion-corrosion regime and wastage maps are developed as $V_p$-$E_{ap}$ diagrams at the given pH and temperature levels, Figure 3(a-d). These Pourbaix diagrams are important in the construction of both 2D and 3D erosion-corrosion maps, as they categorise the behaviour of the metal under specified corrosive conditions (temperature, pH and applied potential).

### *3.1 2-D Erosion-corrosion maps*

The effects of pH variation at elevated temperatures as a function of increasing temperature are illustrated in Figures 4, 5 and 6 for the regime maps and these indicate that there are a range of erosion-corrosion regimes at lower temperatures, with the dissolution affected regions reducing with increasing temperature, Fig. 4 and 5. At pH 9, only at the lowest temperature was dissolution affected behaviour observed, Fig, 6(a). The passivation affected erosion regimes predominated at higher temperatures, Fig. 6. The wastage maps, Figs. 7-8, indicate that the high wastage associated with dissolution affected erosion-corrosion behaviour decreased at pH 5, Fig. 7, as temperature was increased. A similar effect was observed at pH 7, Fig. 8. At pH 9, the effect of temperature was to shift the high wastage regime to lower applied potentials, Fig. 9. To illustrate the variation of ($E_{pas}$) boundary values with the temperature change, Figure 10(a-d) shows the difference in each pH level for the passivity boundaries. From this, it is shown that the ($E_{pas}$) value decreased as the temperature and the pH increased.

### *3.2 3-D Erosion-corrosion maps*

Figures 11 and 12 show the regime maps for Fe at constant applied potentials and various pH values and can be compared to 2-D erosion-corrosion maps generated in previous work[15].

For the erosion-corrosion regime maps at pH 5 and applied potential V= -0.6 [V] (SCE), Fig. 11, the dissolution regimes prevailed. At the pipe bend, in regions of higher particle concentration and velocity, there were transitions to erosion-dissolution and erosion-dominated regimes, Figure 11(a), and these tended to increase as the temperature increased; Figure 11(b-d). This is consistent with the Pourbaix diagrams in these conditions.

In contrast with the results at pH=5, Figure 12(a-d) shows the erosion-corrosion regimes at pH=9 and applied potential V= -0.6 [V] (SCE). Here, the erosion-passivation regime predominated. In these conditions, the corrosion rate decreased on the maps compared to erosion.

The effects of temperatures, at two applied potentials, -0.6 and -0.05 [V] SCE were assessed, Figures 13-14, at pH 7. At pH 7, and at -0.6 [V] (SCE), Figure 13, the erosion dominated regime increased with increasing temperature, where the prevailing erosion-corrosion regime is erosion-dissolution. At a higher potential V= -0.05 [V] (SCE); Figure 14, the erosion-passivation regime which predominated, marginally decreased with increasing temperature.

To illustrate the wastage maps dependence on the pH value, Figures 15 and 16 show the wastage maps for Fe at V= -0.6 [V] (SCE) and pH values 5 and 9 respectively. Although the erosion rate increased as the temperature increased, the wastage maps in Figures 15(a-d)) show a decrease in the high wastage regime as the temperature increased. However, this behaviour was reversed at pH=9; Figure 16(a-d).

The applied potential effect on the wastage maps was investigated in Figures 17 and 18, where the wastage maps for pH= 7 at -0.6 and -0.05 [V] (SCE) are given. Some similarities between the behaviour at -0.6 [V]; Figure 17(a-d), with that in Figure 15(a-d), were observed. For the wastage maps at -0.05 V, the marginally higher wastage regimes were observed at higher temperatures, in contrast with that observed at the lower applied potentials.

## 4. Discussion

It should be noted that all the results for the erosion-corrosion regimes and wastage maps here are within the range of applied potentials used in previous research [15] as are the pH values selected.

Figure 3 shows that, as the temperature increases, the dissolution regions decrease while simultaneously the passivation regions increase. This can be interpreted as the greater tendency of Fe to thermodynamically passivate as the temperature is increased. The pH above which no dissolution occurs shifts to lower values as the temperature is increased. This boundary is represented in Figure 3(a) by the vertical line (5).

### *4.1 2-D Erosion-corrosion maps*

A comparison between the erosion-corrosion regime maps in Figures 4, 5 and 6 with the wastage maps; Figures 7, 8, and 9, shows that, where dissolution prevails, the total wastage of (Fe) is considerably higher than that in the passivation regime. This is because of the high corrosion rates in the case of dissolution. The regime maps also show that, the dissolution regimes areas at pH=5; Figure 4(a-d), are wider than that at higher pH values; Figures 5(a-d) and 6(a-d).

As the temperature is increased at pH=9; Figure 6(b-d), no dissolution regimes are observed, and the passivation regimes predominate. This also affects the wastage maps at this pH value; Figure 9(b-d), where ascending wear rate from low to high regions are observed as the extent of erosion-passivation increases. This is contrary to what is observed for Figures 7 and 8(a, b), where the high wastage region predominates at intermediate potentials due to dissolution corrosion and since the wastage rates for dissolution corrosion tend to be higher than for passivation, there is a very different mode of wastage behaviour in such conditions, with the rate of wastage decreasing with increasing temperature.

### *4.2 3-D Erosion-corrosion maps*

It is important to note that the 3-D map for Fe will exhibit many erosion-corrosion regimes because of the changes of velocity and particle frequency of impact over the component. The areas thus dominated by these regimes will change significantly as these parameters change.

The effect of increasing pH from 5 to 9, Figures 11 and 12, has an important influence on the corrosion mechanism that controls the degradation rate for the Fe. The same effect is also observed when changing the applied potential in the positive direction; Figures 13 and 14. The corrosion mechanism is changed from dissolution to passivation domination affected behaviour over the component.

Increases in temperature have accordingly a significant effect on the erosion-corrosion regime maps. It is observed that at pH 5, Fig. 11, Fe exhibits various erosion-corrosion regimes predominating. This is in contrast with the results at high pH value where a stable erosion-passivation regime is spread on the pipe surface, Fig. 12.

The increase in erosion dominated behaviour as a function of increasing temperature is clearly demonstrated at low applied potentials, Fig. 13 (a-d). Figure 14(a-d) shows similar but not identical maps on the pipe surface at each temperature level when comparing with the erosion-passivation maps in Figure 12(a-d)). The passivation-erosion regime is dominant on the straight ends of the pipe, while the erosion-passivation regime remains dominant in the pipe bend regions. The marginally higher evidence of passivation affected regimes, at lower temperatures, is due to the lower erosion rate at such temperatures, and the fact that the dissolution regime disappears at the higher temperatures.

Contrary to the behaviour exhibited by the erosion-corrosion regime maps, there is only slight effect of temperature on the wastage maps at all pH and applied potential values, Figures 15-18, with very little difference in the maximum wastage, under this window of conditions.

There are several limitations of this approach to date. The model assumes no effect of corrosion on erosion which is simplistic. The kinetics of re-passivation with temperature have not been accounted for due to the very low rates of growth involved and the narrow temperature range. It is acknowledged that over a wider temperature range, such effects may have to be considered.

The model assumes that the substrate properties change with temperature but not do not consider such effects for the mechanical properties of the film. This is also a simplistic assumption.

Nonetheless such issues above, this technique is a powerful new technique for the study of the influence of many of the parameters acting simultaneously in the erosion-corrosion process. It can predict the regions of severe wear due to the additive effect of erosion and corrosion, as well as the rate of metal degradation. Further work will to address those issues above, in addition to assessing the effects of other variables and additional materials in both 2-D and 3-D formats.

## 5. Conclusions

(i) The effect of temperature has been assessed for the erosion-corrosion of Fe in aqueous conditions

(ii) The results have indicated that the passivation potential decreased with increasing temperature whereas the erosion of the substrate increased

(iii) Transitions between erosion-corrosion regimes were observed as a function of increasing temperature

(iv) Two and three dimensional erosion-corrosion maps were constructed based on the results showing the wide range of erosion-corrosion regimes possible in such conditions.

## 6. References


[1] H. C. Meng, K. C. Ludema, Wear models and predictive equations: their form and content,Wear 181-183 (Part 2), (1995), 443–457.

[2] R. W. Lyczkowski, J. X. Bouillard, State-of-the-art review of erosion modeling in fluid/solids systems, Progress in Energy and Combustion Science, 28 (6), (2002), 543–602.

[3] D. Chen, M. Sarumi, S. T. S. Al-Hassani, S. Gan, Z. Yin, A model for erosion at normal impact, Wear 205 (1-2), (1997), 32–39.

[4] D. J. O'Flynn, M. S. Bingley, M. S. A. Bradley, A. J. Burnett, A model to predict the solid particle erosion rate of metals and its assessment using heat-treated steels, Wear 248 (1-2), (2001), 162 – 177.

[5] B. E. Lee, C. A. J. Fletcher, M. Behnia, Computational study of solid particle erosion for a single tube in cross flow, Wear 240 (1-2), (2000), 95–99.

[6] M. M. Stack, F. H. Stott, G. C. Wood, Review of mechanisms of erosion-corrosion of alloys at elevated temperature, Wear 162, (1993), 706–712.

[7] M. Yovanovich, Micro and macro hardness measurements, correlations, and contact models., in: Proceedings of 44th AIAA Aerospace Sciences Meeting and Exhibition, no. 979, Reno, Nevada, USA., 2006.

[8] H. Argeso, A. N. Eraslan, On the use of temperature-dependent physical properties in thermomechanical calculations for solid and hollow cylinders, International Journal of Thermal Sciences 47, (2008), 136–146.

[9] E. Gileadi, E. Eisner, Some observations concerning the tafel equation and its relevance to charge transfer in corrosion, Corrosion Science 47, (2005), 3068–3085.

[10] P. S. Glockner, G. F. Naterer, Near-wall velocity profile with adaptive shape functions for turbulent forced convection, International Communications in Heat and Mass Transfer 32 (1-2), (2005), 72 – 79.

[11] D. Cubicciotti, Potential ph diagrams for alloy water-systems under lwr conditions, Journal of Nuclear Materials 201, (1993), 176–183.

[12] M. M. Stack, L. Bray, Interpretation of wastage mechanisms of materials exposed to elevated temperature erosion-corrosion using erosion-corrosion maps and computer graphics, Wear 186 (1), (1995), 273–283.

[13] M. M. Stack, Q. Songroehrle, F. H. Stott, G. C. Wood, Computer simulation of erosion-corrosion interaction at elevated temperature, Wear 181, (1995), 516–523.

[14] M. Stack, S. Abdelrahman, B. Jana, A new methodology for modeling erosion-corrosion regimes on real surfaces: Gliding down the galvanic series for a range of metal-corrosion systems, Wear 268 (3-4), (2010), 533 – 542.

[15] M. M. Stack, B. D. Jana, Modeling particulate erosion-corrosion in aqueous slurries: some views on the construction of erosion-corrosion maps for a range of pure metals, Wear 256 (9-10), (2004), 986–1004.

[16] R. J. K. Wood, T. F. Jones, J. Ganeshalingam, N. J. Miles, Comparison of predicted and experimental erosion estimates in slurry ducts, Wear 256 (9-10), (2004), 937–947.

[17] G. Sundararajan, P. G. Shewmon, A new model for the erosion of metals at normal incidence, Wear 84 (2), (1983), 237–258.

[18] G. L. Sheldon, A. Kanhere, Investigation of impingement erosion using single particle, Wear 21 (1) (1972) 195–&.

[19] K. M. Nho, Experimental investigation of heat flow rate and directional effect on contact conductance of anisotropic ground/lapped interfaces, Ph.D. thesis, University of Waterloo, Canada (1990).

[20] S. K. Das, K. M. Godiwalla, S. Shubha, S. P. Mehrotra, P. K. Dey, A mathematical model to characterize effect of silica content in the boiler fly ash on erosion behaviour of boiler grade steel, Journal of Materials Processing Technology 204 (1-3), (2008), 239–247.

[21] Y. Shida, H. Fujikawa, Particle erosion behavior of boiler tube materials at elevated temperature, Wear 103 (4), (1985), 281–296.

[22] D. R. Lide (Ed.), CRC Handbook of Chemistry and Physics, 87th Edition, Taylor and Francis, Boca Raton, FL, USA, (2007), Ch. Properties of Solids, Ch.12, p. 195, CD-ROM Version.

[23] G. Sundararajan, A comprehensive model for the solid particle erosion of ductile materials, Wear 149 (1-2), (1991), 111 – 127.

[24] A. Forder, M. Thew, D. Harrison, A numerical investigation of solid particle erosion experienced within oilfield control valves, Wear 216 (2), (1998), 184–193.

[25] M. M. Stack, N. Corlett, S. Zhou, Some thoughts on the effect of elastic rebounds on the boundaries of the aqueous erosion-corrosion map, Wear 214 (2), (1998), 175–185.

[26] Y. Orcan, A. N. Eraslan, Thermal stresses in elastic-plastic tubes with temperature-dependent mechanical and thermal properties, Journal of Thermal Stresses 24 (11), (2001), 1097–1113.

[27] A. N. Eraslan, Y. Orcan, Computation of transient thermal stresses in elastic-plastic tubes: Effect of coupling and temperature-dependent physical properties, Journal of Thermal Stresses 25 (6), (2002), 559-572.

[28] N. Noda, Thermal stresses in materials with temperature dependent properties, in: Proceedings of the NATO Advanced Research Workshop on Thermal Shockand Thermal Fatigue Behaviour of Advanced Ceramics, Kluwer Academic, MA, USA, (1993), pp. 15–26.

[29] D. R. Lide (Ed.), CRC Handbook of Chemistry and Physics, 87th Edition, Taylor and Francis, Boca Raton, FL, USA, (2007), Ch. Fluid Properties, Ch.6, p. 2, CD-ROM Version.

[30] FLUENT, Inc., FLUENT user's guide, Version 6.3 (2006).

[31] R. J. K. Wood, T. F. Jones, Investigations of sand-water induced erosive wear of AISI 304l stainless steel pipes by pilot-scale and laboratory-scale testing, Wear 255 (1), (2003), 206–218.

[32] M. Pourbaix, Atlas of Electrochemical Equilibria in Aqueous Solutions, Pergamon Press, Oxford, New York, (1966).

[33] Y. Tirupataiah, B. Venkataraman, G. Sundararajan, The nature of the elastic rebound of a hard ball impacting on ductile metallic target materials, Materials Science and Engineering a: Structural, Materials Properties, Microstructure, and Processing 124 (2), (1990), 133–140.

[34] M. M. Stack, N. Corlett, S. Zhou, A methodology for the construction of the erosion-corrosion map in aqueous environments, Wear 203, (1997), 474–488.

[35] M. J. Graham, J. A. Bardwell, G. I. Sproule, D. F. Mitchell, B. R. MacDougall, The growth and stability of passive films, Corrosion Science 35, (1993), 13 – 18.

[36] B. Stellwag, The mechanism of oxide film formation on austenitic stainless steels in high temperature water, Corrosion Science 40 (2-3) (1998) 337 – 370.

[37] B. T. Lu, J. L. Luo, F. Mohammadi, K. Wang, X. M. Wan, Correlation between repassivation kinetics and corrosion rate over a passive surface in flowing slurry, Electrochimica Acta 53 (23), (2008), 7022–7031.

## 6. List of Figures

## 7. List of tables

l. [31] . . . . . .

Table 1: The equations of boundary lines between the passive and dissolution regions see Figure 3(a).

| Line | Temperature [$K$] | Equation |
|---|---|---|
| Line 1 | 298 | E= -0.618 |
| | 323 | E= -0.617 |
| | 343 | E= -0.618 |
| | 363 | E= -0.620 |
| Line 2 | 298 | E= 0.771 |
| | 323 | E= 0.814 |
| | 343 | E= 0.848 |
| | 363 | E= 0.879 |
| Line 3 | 298 | E= 1.076 - 0.177 pH |
| | 323 | E= 1.097 - 0.192 pH |
| | 343 | E= 1.119 - 0.204 pH |
| | 363 | E= 1.144 - 0.216 pH |
| Line 4 | 298 | E= -0.054 - 0.059 pH |
| | 323 | E= -0.046 - 0.064 pH |
| | 343 | E= -0.039 - 0.068 pH |
| | 363 | E= -0.032 - 0.072 pH |
| Line 5 | 298 | pH = 1.72 |
| | 323 | pH = 1.47 |
| | 343 | pH = 1.33 |
| | 363 | pH = 1.23 |

Table 2: CFD modelling equations, operating and boundary conditions

| Model parameter | Water | Alumina sand |
|---|---|---|
| Solver equations | Navier-Stokes | DPM |
| Turbulence model | Standard $k$ $\varepsilon$ | |
| Wall treatment | Standard wall functions | |
| Coupling | | two-way coupling |
| operating conditions | ambiant | |
| inlet velocity [m $s^{-1}$] | 3 | 3 |

Table 3: Physical and mechanical properties for the slurry and target material

| | Fluid (water) | Sand (alumina) | Target (mild steel) |
|---|---|---|---|
| density [kg $m^{-3}$] | 998 | 2670 | 7850 |
| particle size [m] | | $10^{-3}$ | |
| mass flow rate[kg $s^{-1}$] | 14.3 | 3.827 | |

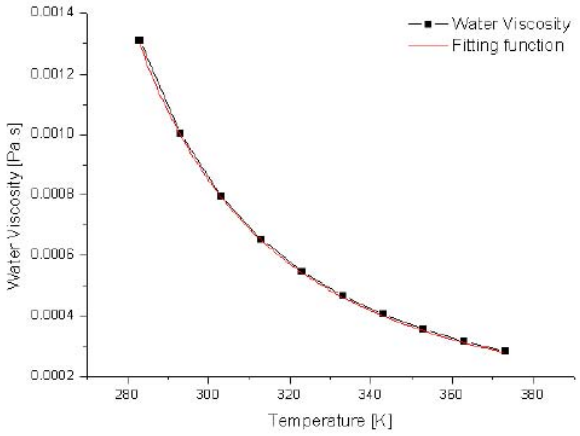


Figure 1: Variation of water viscosity with temperature and the curve fitting function.

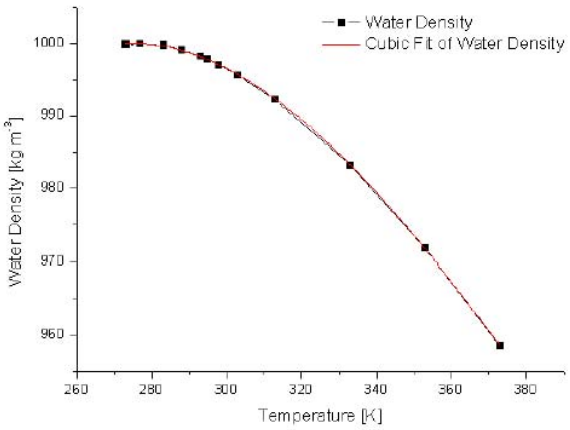


Figure 2: Variation of water density with temperature and the curve fitting function.

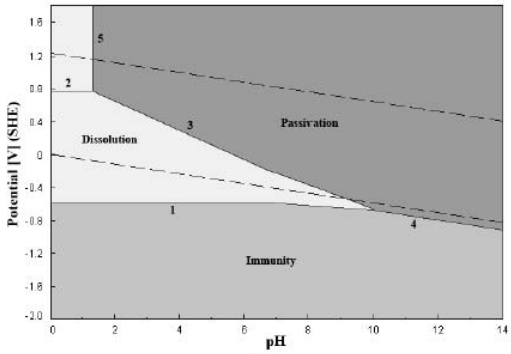


(a)

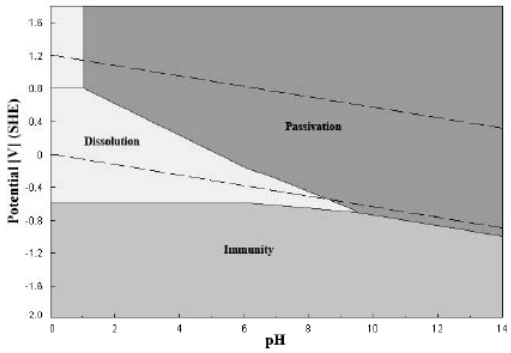


(b)

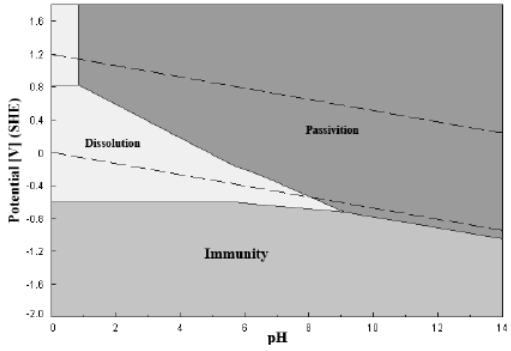


(c)

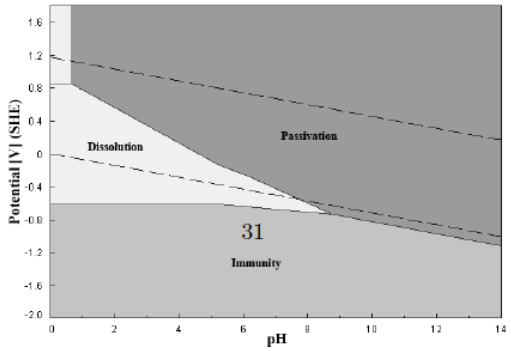


(d)

Figure 3: Simplified Pourbaix diagrams for the Fe-water system at : (a)298, (b)323 (c)343 (d)363 [K].

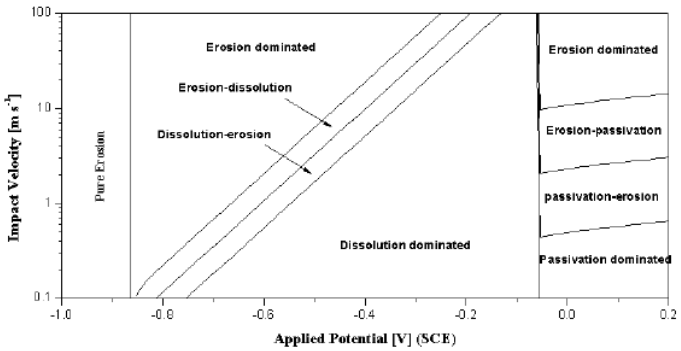


(a)

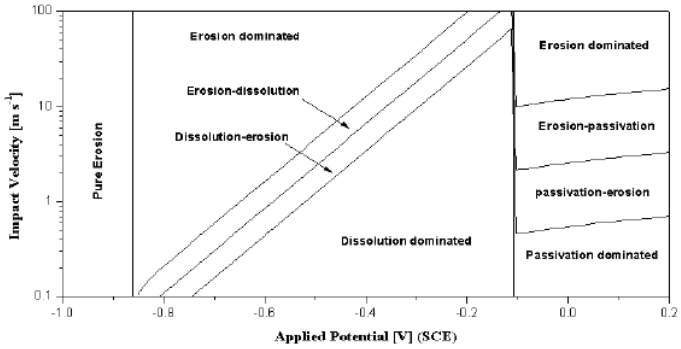


(b)

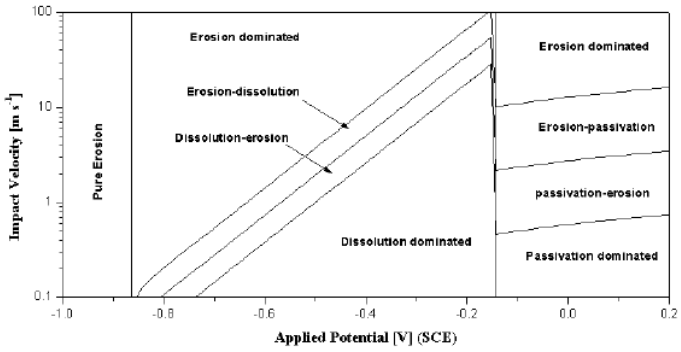


(c)

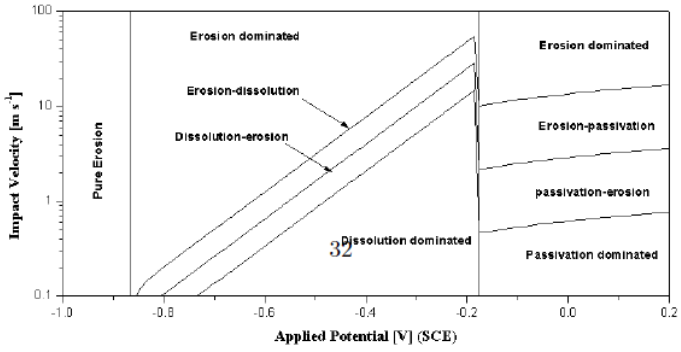


(d)

Figure 4: Regime maps for Fe at pH 5 and: (a) 298, (b) 323, (c) 343, and (d) 363 [K].

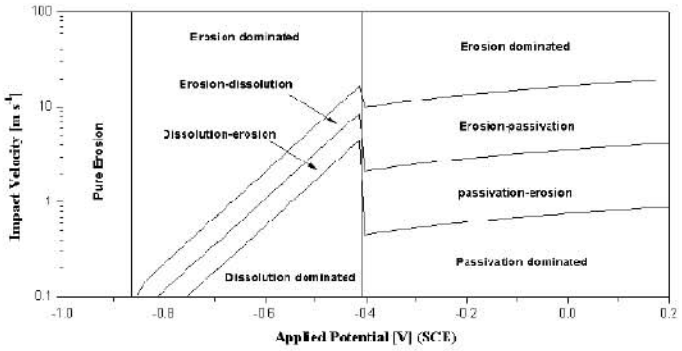


(a)

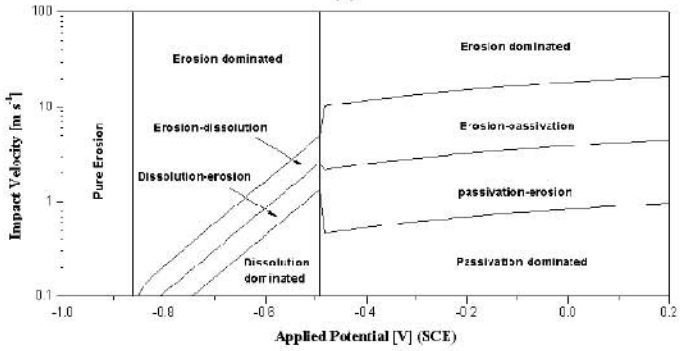


(b)

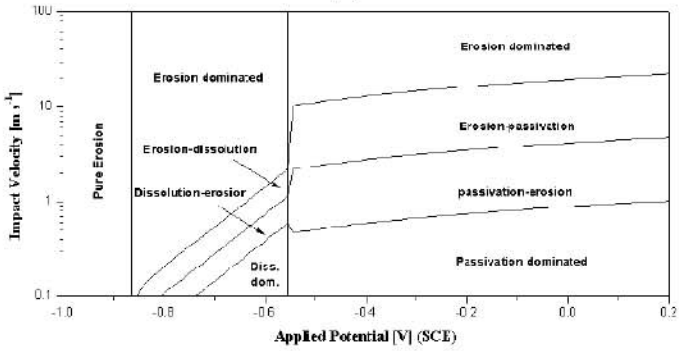


(c)

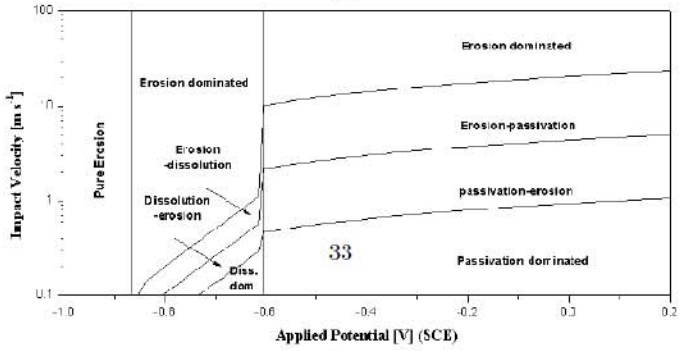


(d)

Figure 5: Regime maps for Fe at pH 7 and: (a) 298, (b) 323, (c) 343, and (d) 363 [K].

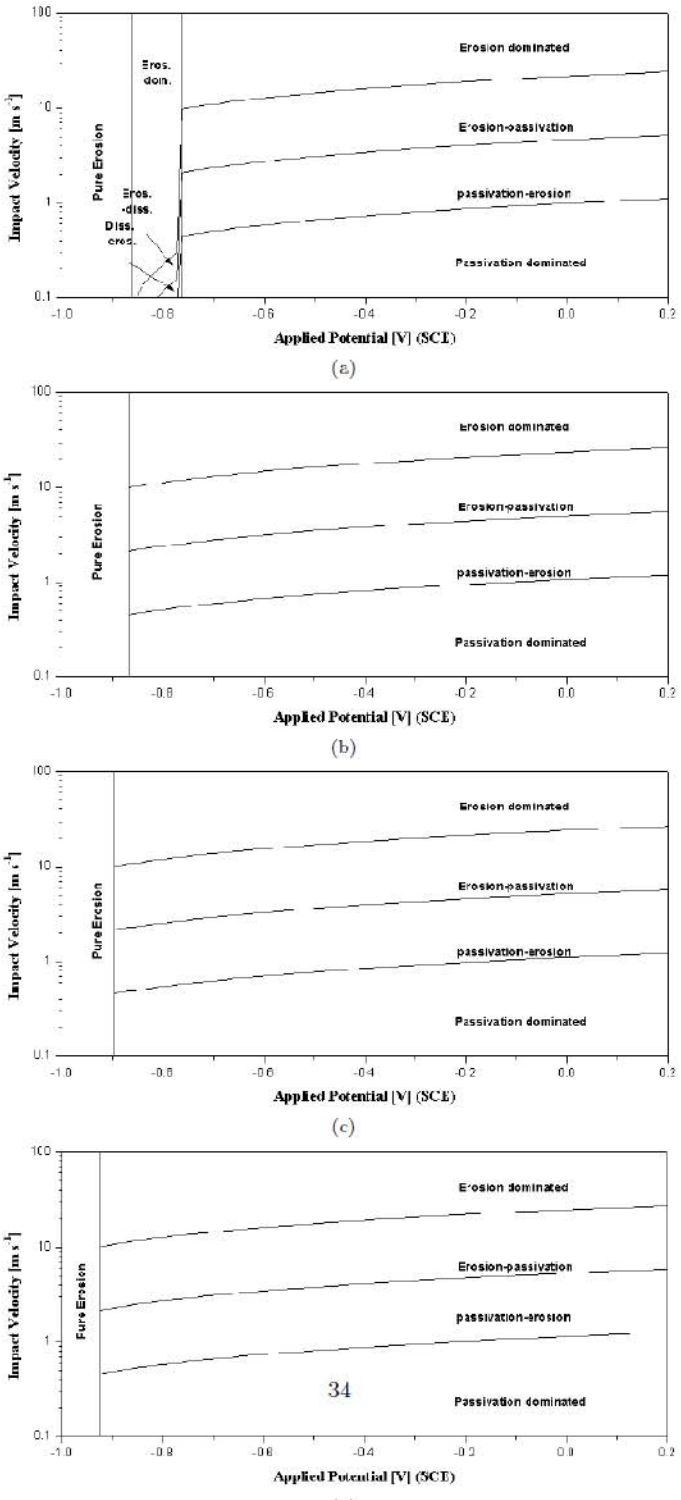


Figure 6: Regime maps for Fe at pH 9 and: (a) 298, (b) 323, (c) 343, and (d) 363 [K].

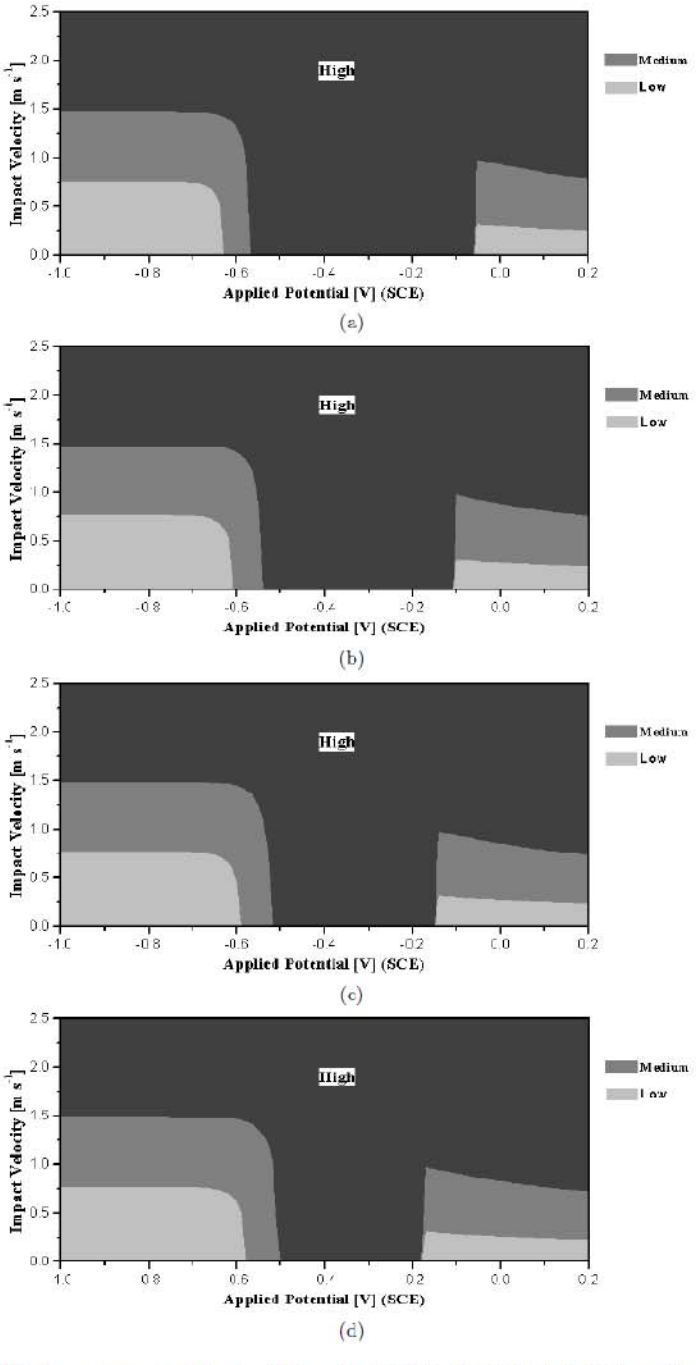


Figure 7: Wastage maps for Fe at pH 5 and; (a) 298, (b) 323, (c) 343, and (d) 363 [K].

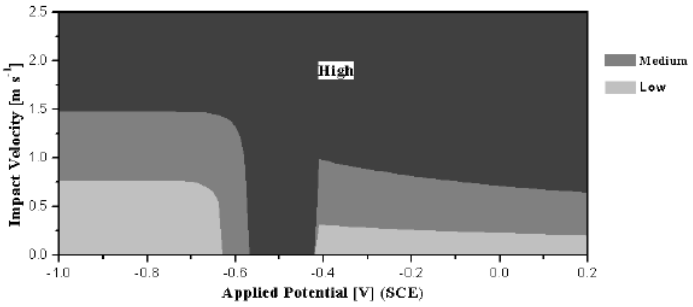


(a)

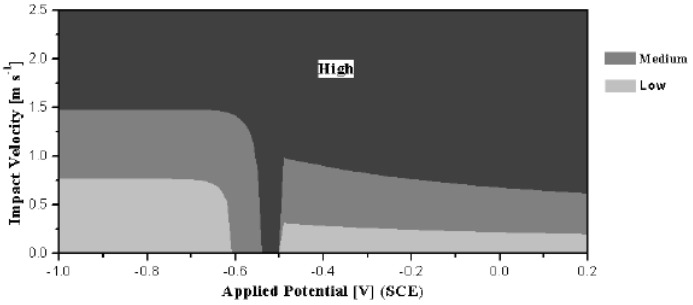


(b)

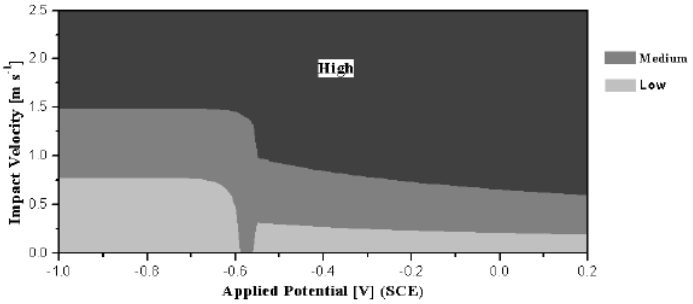


(c)

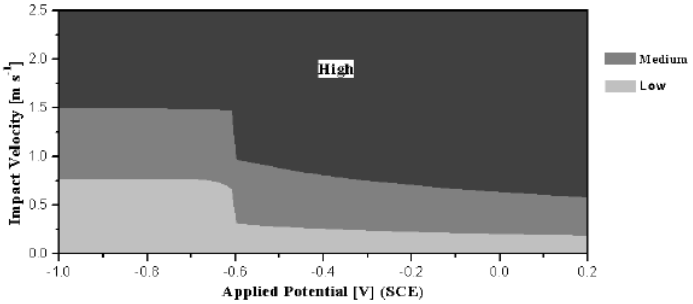


(d)

Figure 8: Wastage maps for Fe at pH 7 and: (a) 298, (b) 323, (c) 343, and (d) 363 [K].

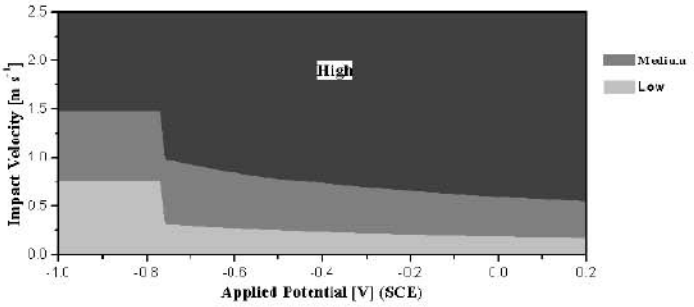


(a)

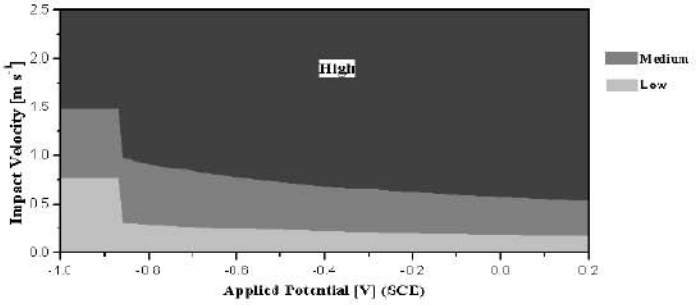


(b)

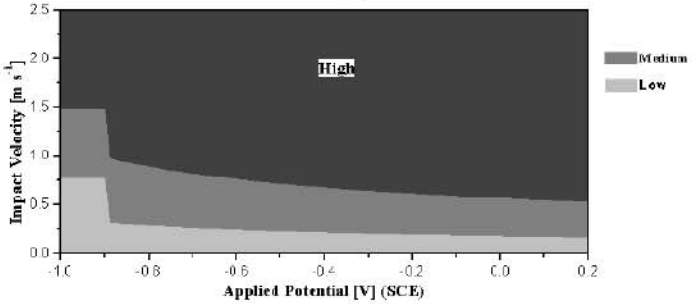


(c)

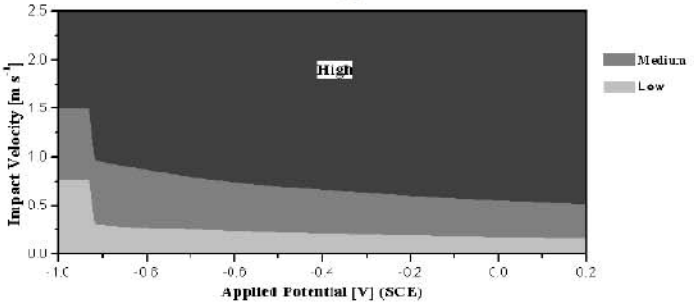


(d)

Figure 9: Wastage maps for Fe at pH 9 and (a) 298, (b) 323, (c) 343, and (d) 363 [K].

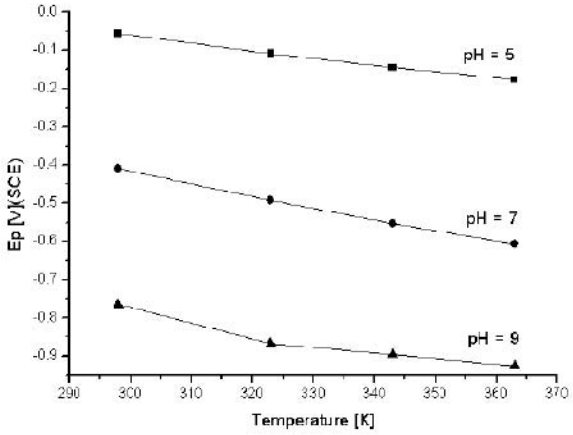


Figure 10: Variation of $E_{pas}$ value with Temperature at different pH values.

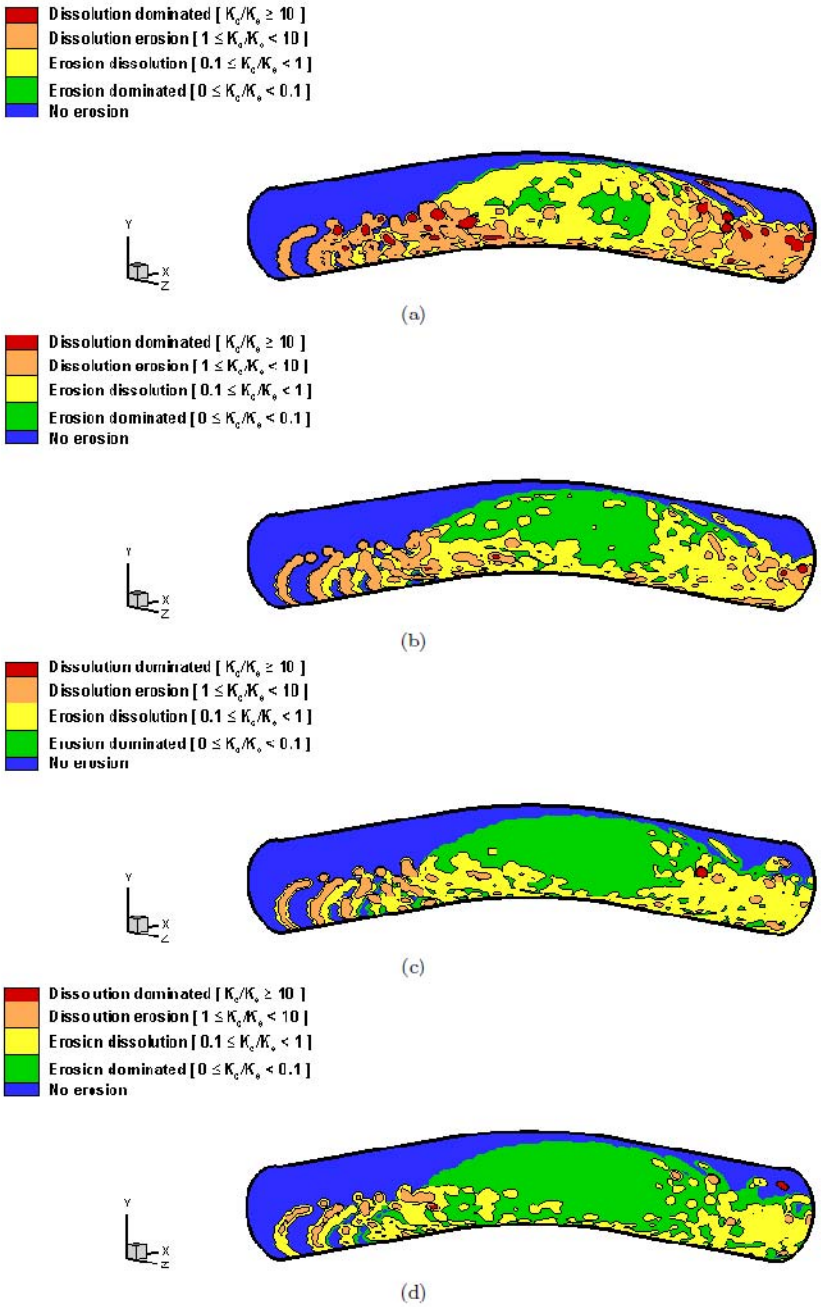


Figure 11: Regime maps for Fe at pII 5, V= -0.6 [V](SCE) at:(a) 298, (b) 323, (c) 343, (d) 363 [K].

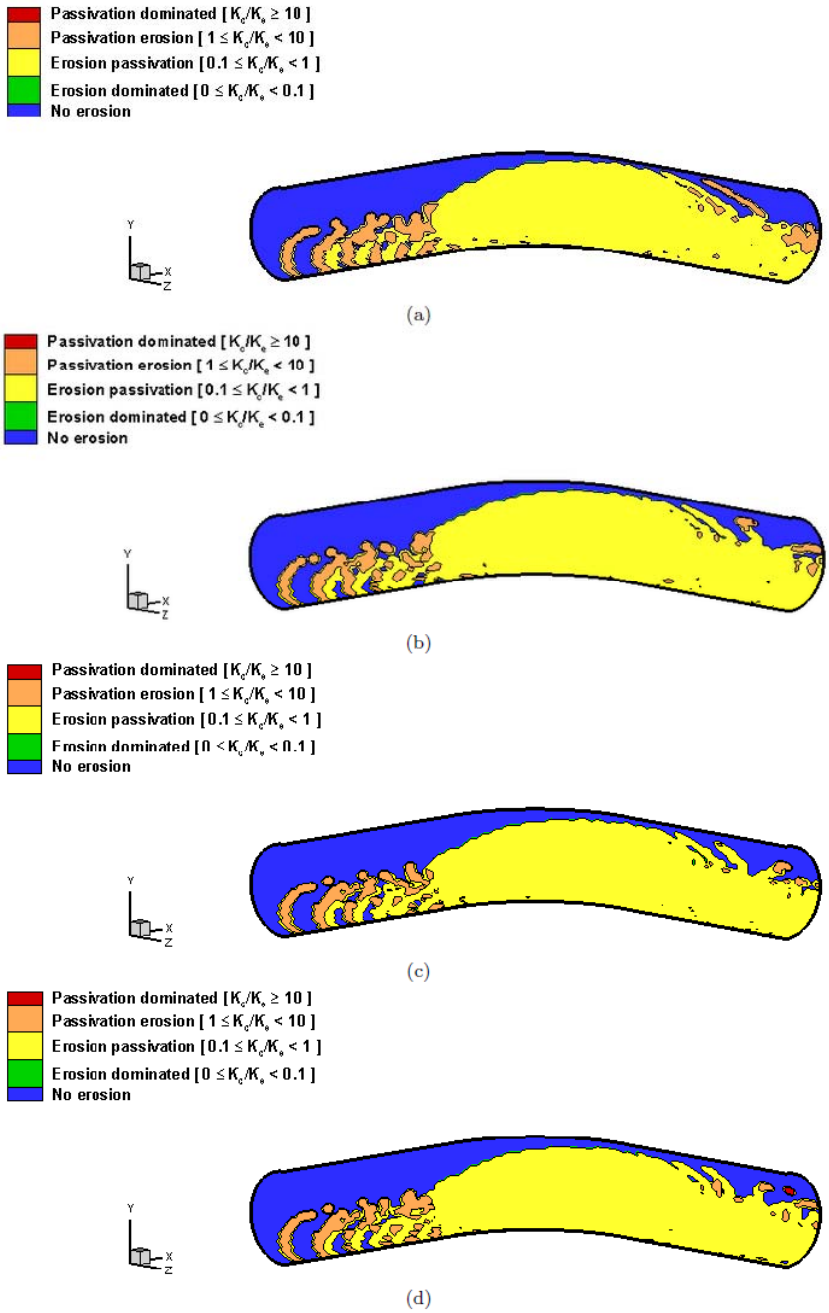


Figure 12: Regime maps for Fe at pH 9, V= -0.6 [V](SCE) at:(a) 298, (b) 323, (c) 343, (d) 363 [K].

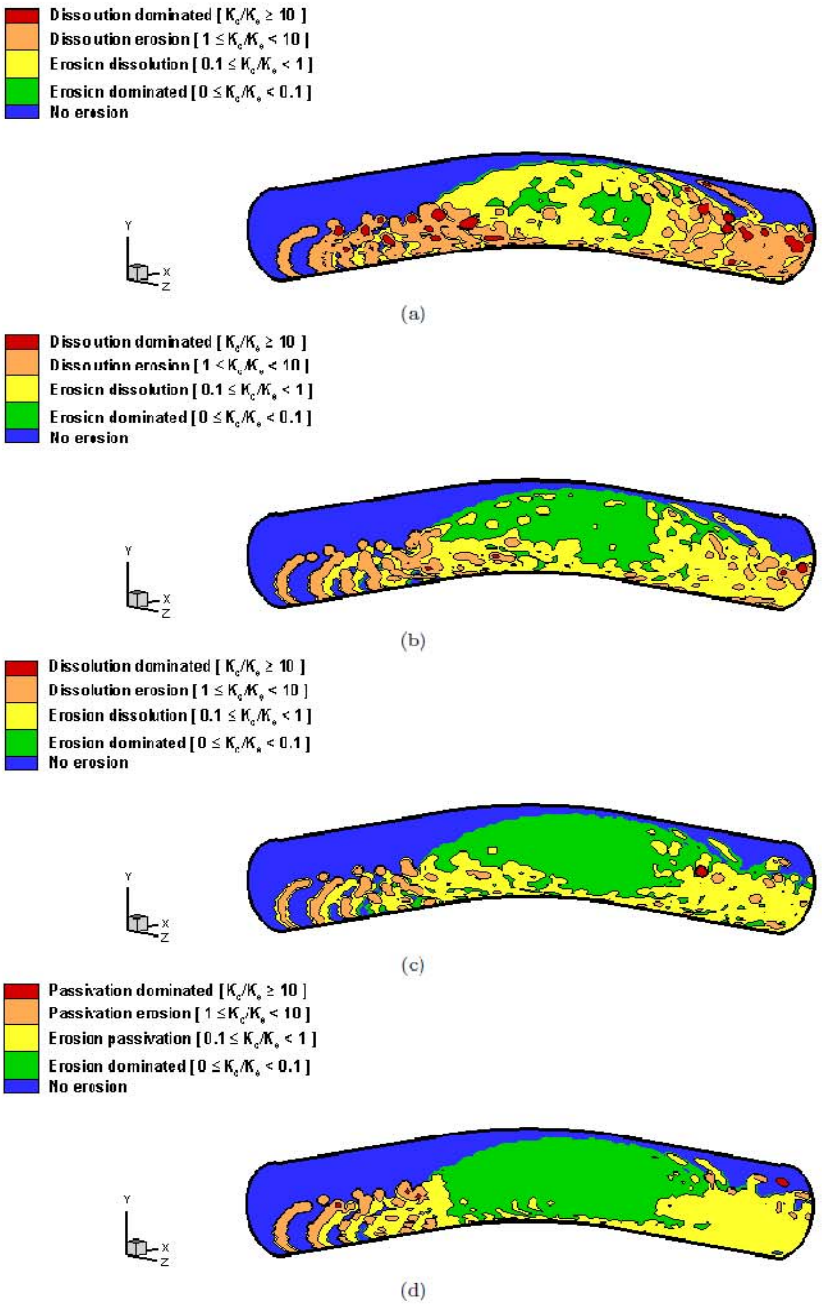


Figure 13: Regime maps for Fe at pH 7, V= -0.6 [V](SCE) at:(a) 298, (b) 323, (c) 343, (d) 363 [K].

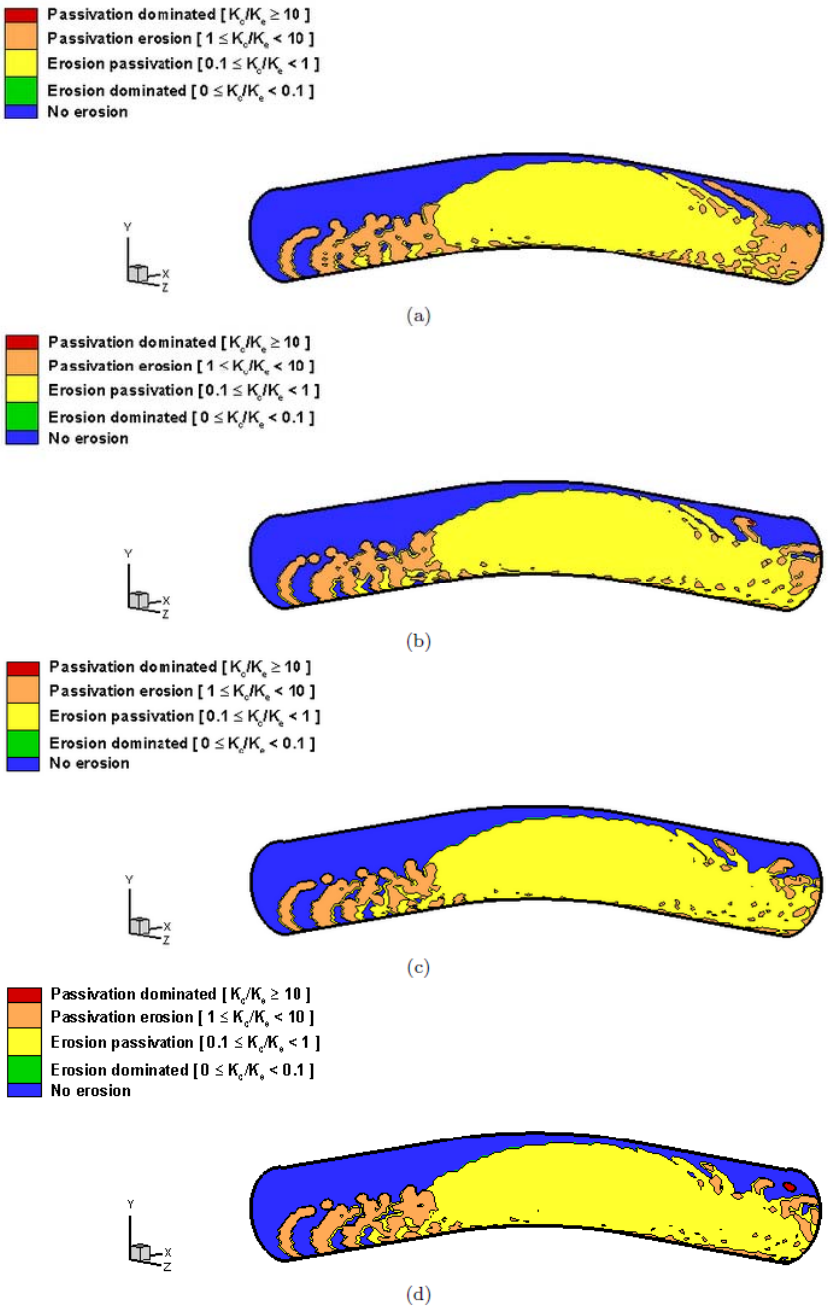


Figure 14: Regime maps for Fe at pH 7, V= -0.05 [V](SCE) at:(a) 298, (b) 323, (c) 343, (d) 363 [K].

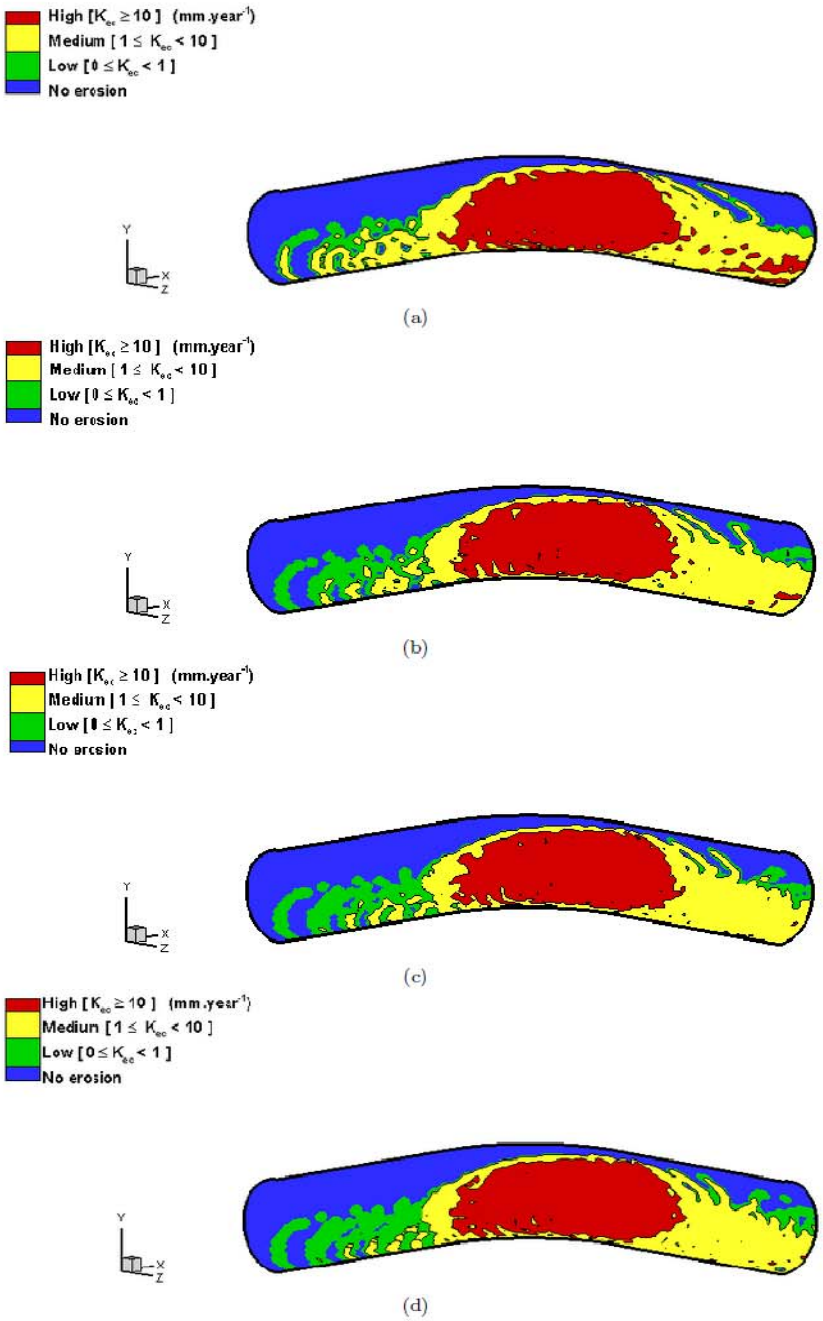


Figure 15: Wastage maps for Fe at pH 5, V= -0.6 [V](SCE) at:(a) 298, (b) 323, (c) 343, (d) 363

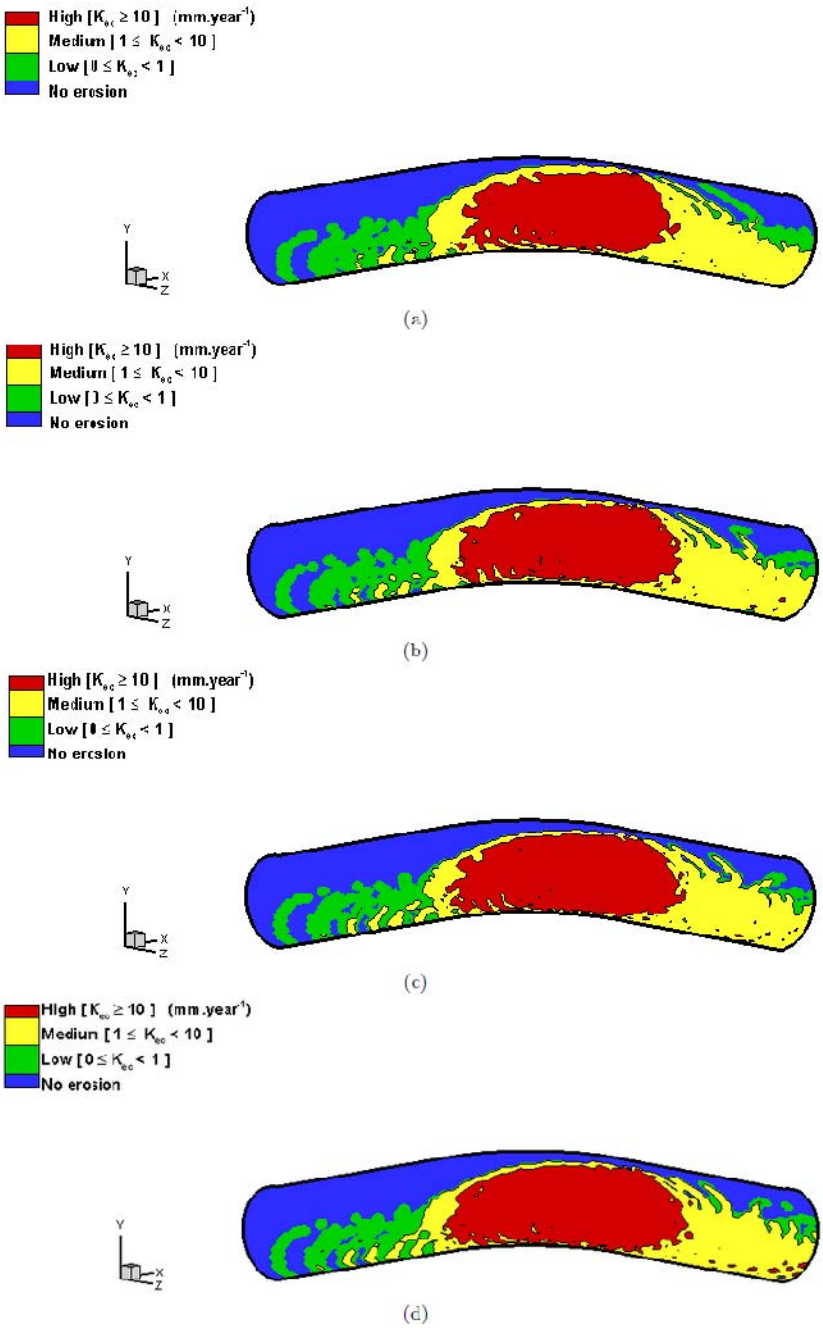


Figure 16: Wastage maps for Fe at pII 9, V= -0.6 [V](SCE) at:(a) 298, (b) 323, (c) 343, (d) 363

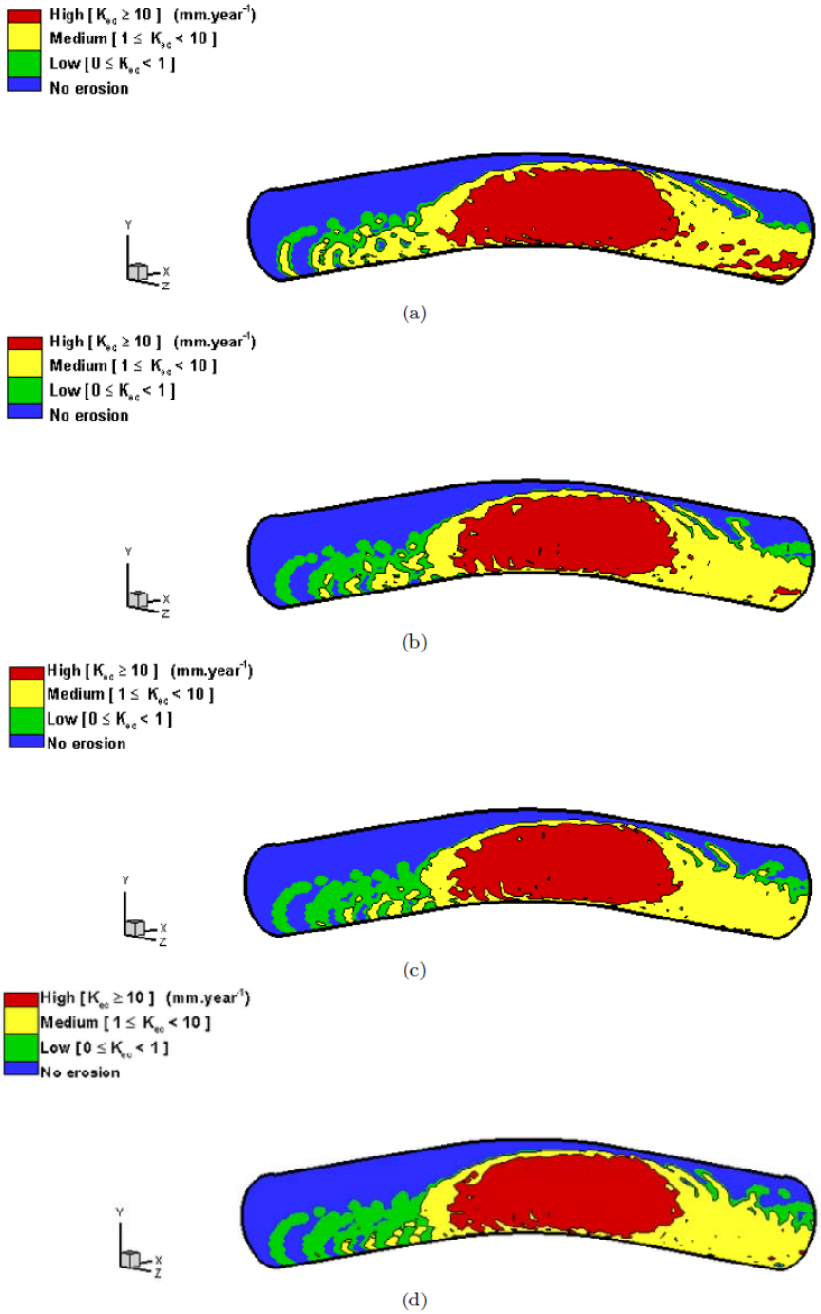


Figure 17: Wastage maps for Fe at pH 7, V= -0.6 [V](SCE) at:(a) 298, (b) 323, (c) 343, (d) 363

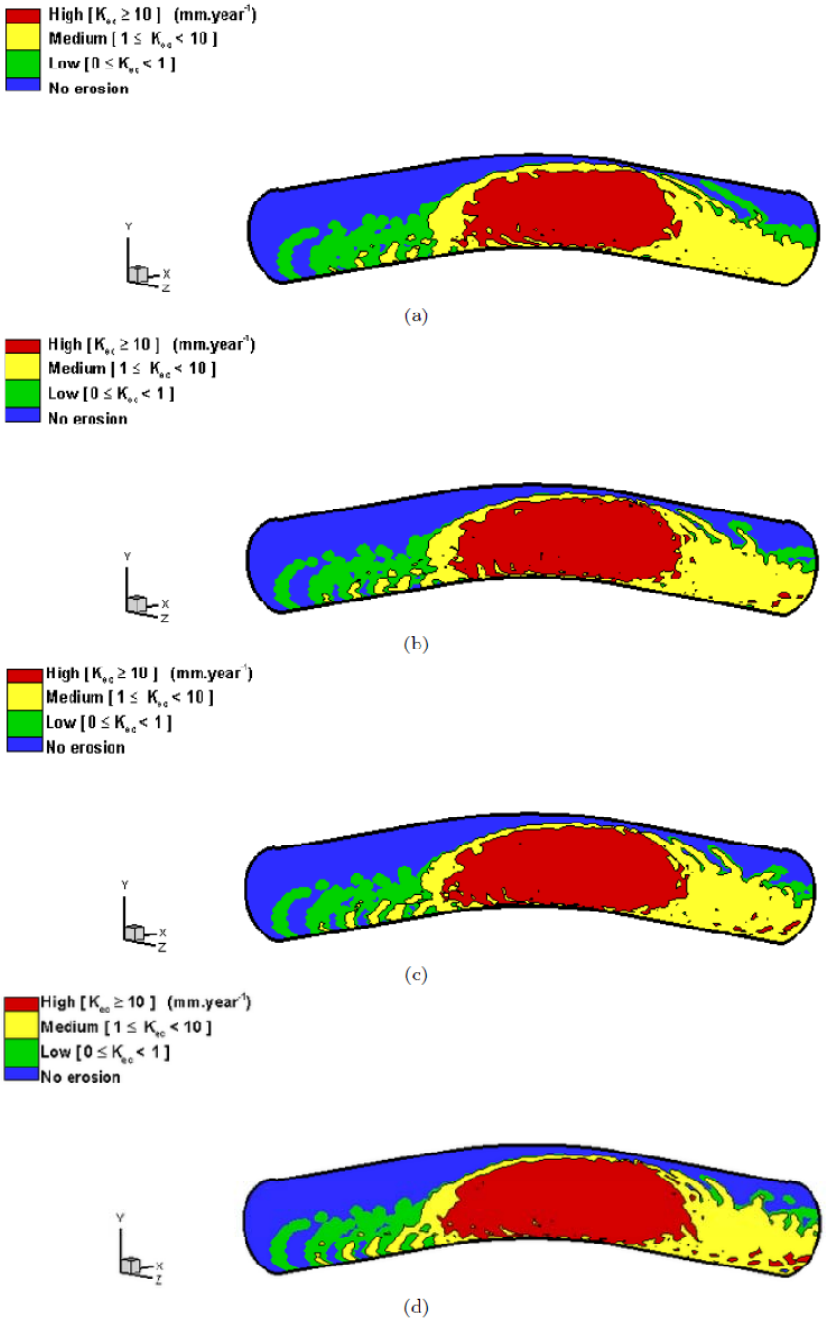


Figure 18: Wastage maps for Fe at pII 7, V– -0.05 [V](SCE) at:(a) 298, (b) 323, (c) 343, (d) 363